ACS APPLIED MATERIALS & INTERFACES

Research Article

www.acsami.org

Understanding Charge Transfer in Carbon Nanotube–Fullerene Bulk Heterojunctions

Maogang Gong,[†,&] Tejas A. Shastry,[‡,&] Qiannan Cui,[§] Ryan R. Kohlmeyer,[∥,⊥] Kyle A. Luck,[‡] Andrew Rowberg,[‡] Tobin J. Marks,[‡,#] Michael F. Durstock,[⊥] Hui Zhao,[§] Mark C. Hersam,*[,‡,#] and Shenqiang Ren*[,†]

[†]Department of Chemistry and [§]Department of Physics and Astronomy, University of Kansas, Lawrence, Kansas 66045, United States

[‡]Department of Materials Science and Engineering and [#]Department of Chemistry, Northwestern University, Evanston, Illinois 60208, United States

[∥]National Research Council, Washington, D.C. 20001, United States

[⊥]Soft Matter Materials Branch, Materials and Manufacturing Directorate, Air Force Research Laboratory, Wright-Patterson Air Force Base, Ohio 45433, United States

Supporting Information

ABSTRACT: Semiconducting single-walled carbon nanotube/fullerene bulk heterojunctions exhibit unique optoelectronic properties highly suitable for flexible, efficient, and robust photovoltaics and photodetectors. We investigate charge-transfer dynamics in inverted devices featuring a polyethylenimine-coated ZnO nanowire array infiltrated with these blends and find that trap-assisted recombination dominates transport within the blend and at the active layer/nanowire interface. We find that electrode modifiers suppress this recombination, leading to high performance.

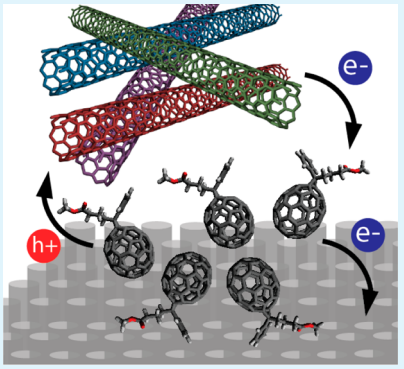

KEYWORDS: *nanocarbon, fullerenes, bulk heterojunction, charge transfer, mechanism*

1. INTRODUCTION

Low-dimensional carbon allotropes, including single-walled carbon nanotubes (SWCNTs) and fullerene derivatives, have been studied extensively in the past decade due to their superlative physical and chemical properties that offer significant potential for thin-film photovoltaics,[1−6] optoelectronics,[7−9] capacitors,[10,11] thermoelectrics,[12] and wearable devices.[13−15] Nanocarbon bulk heterojunctions (BHJs) consisting of electron-donating semiconducting single-walled carbon nanotubes (s-SWCNTs) and electron-accepting fullerenes have attracted much attention due to their broadband spectral photoabsorption, high carrier mobility, and robust chemical, thermal, and mechanical stability.[16−19] Recent advances in device architecture and material processing have enabled the production of SWCNT–fullerene BHJ devices exhibiting superior photodetection and photovoltaic performance.[20,21] However, the charge-transfer dynamics between SWCNTs and fullerenes remains unclear in these novel architectures, and understanding these dynamics will be crucial to further advance their performance for renewable energy and sensing applications.

In this work, we demonstrate inverted SWCNT–fullerene BHJ devices that match or exceed the photovoltaic and photodetection performance of previous devices and use them as platforms to characterize charge-transfer dynamics. Using light-induced electron paramagnetic resonance, light-intensity-dependent current–voltage scans, and ultrafast pump–probe techniques, we study charge-transfer dynamics within the SWCNT–fullerene blend at the interfaces between the active layer and the electrodes, and at the complex interfaces involved in the nanostructured electron transport layer (ETL). Our results reveal that trap-assisted recombination dominates charge transfer within the SWCNT–fullerene blend and at the ETL/active layer interface, in contrast to bimolecular recombination commonly observed in organic and organic–inorganic hybrid photovoltaics.[22−24] We further delineate the interfacial parameters necessary for maintaining high voltage and high current in these devices and identify several areas for future improvement of device performance.

Received: February 18, 2015
Accepted: March 23, 2015
Published: March 23, 2015

DOI: 10.1021/acsami.5b01536
ACS Appl. Mater. Interfaces 2015, 7, 7428−7435

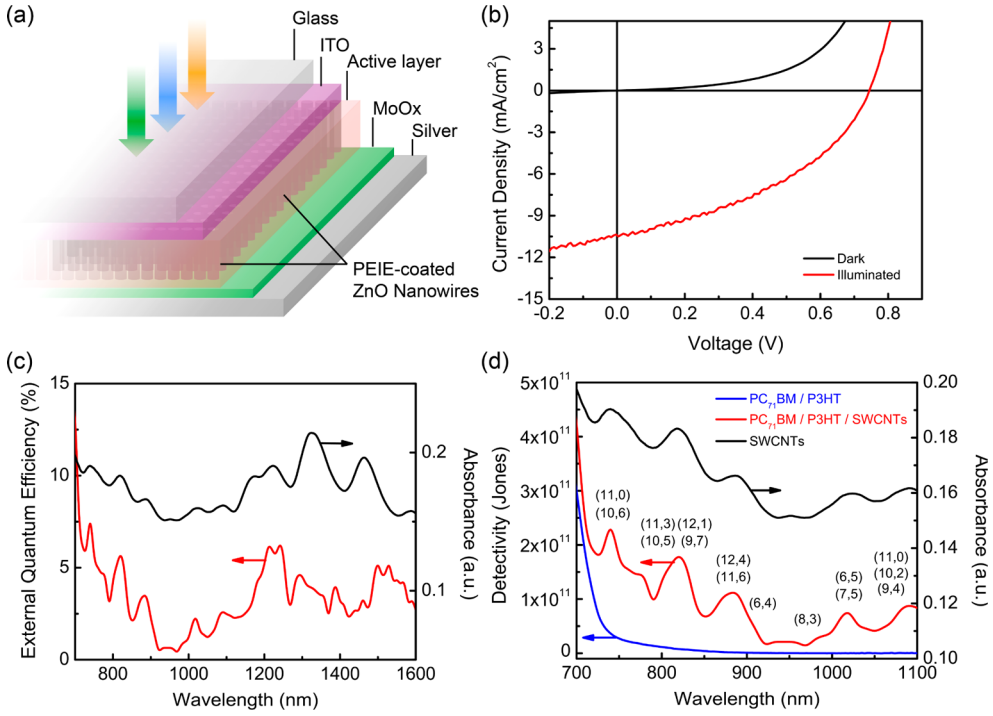

Figure 1. High-performance inverted SWCNT−fullerene photovoltaics and photodetectors. (a) Schematic architecture of the SWCNT−fullerene BHJ device incorporating a ZnO nanowire array as the ETL. (b) Dark and illuminated current−voltage sweeps of the device in (a). (c) Absorbance and external quantum efficiency (EQE) of the device in (a), with a response in the visible regime from the fullerene and in the NIR regime from the SWCNTs. (d) Absorbance and detectivity of the device in (a) plotted against the detectivity of a device without SWCNTs. A marked response is seen in the NIR from multiple SWCNT chiralities denoted by their chiral indices (n,m).

2. EXPERIMENTAL SECTION

Electron Paramagnetic Resonance (EPR) Measurements. Samples were prepared inside a nitrogen-filled glovebox and were dissolved in 1,2-dichlorobenzene (1,2-DCB). After the samples were stirred overnight, 200 μL of testing solution was added to a quartz EPR sample tube within the glovebox. EPR measurements were carried out on an EMX spectrometer at 9.4 GHz at 5 K in an Oxford ESR900 cryostat.

Preparation of ZnO Nanowire Arrays. Prepatterned indium tin oxide (ITO) glass substrates (0.25 in^2, 20 Ω/sq., Thin Film Devices) were cleaned by ultrasonic treatment in aqueous detergent (Alconox), deionized water (DI water), acetone, and isopropyl alcohol sequentially, followed by a UV-ozone treatment. ZnO nanowires were grown on the ITO substrates by a two-step method previously reported.[25] ZnO seed layers were prepared by spin-coating 0.3 M zinc acetate and ethanolamine in 2-methoxyethanol and annealing at 180 °C for 10 min in an N_2 atmosphere. This process was repeated twice followed by annealing in air at either 350 °C for 30 min or 400 °C for 1 h to form a uniform seed layer. The substrates were subsequently immersed into the nanowire growth solution in an autoclave for 60, 90, 120, and 210 min at 95 °C. The growth solution has equal concentration (0.025 M) of zinc acetate and hexamethylenetetramine in DI water. As-grown ZnO nanowire array substrates were thoroughly rinsed with DI water and isopropanol, annealed at 300 °C for 30 min, and briefly sonicated to remove larger nanowires.

SWCNT Solution Preparation. Semiconducting single-walled carbon nanotubes were prepared from solutions of HiPco SWCNTs (NanoIntegris) sonicated in 1% (w/v) sodium cholate in deionized water by a 0.125 in. tip horn ultrasonicator at 12 W for 60 min. Solutions were subsequently sorted by electronic type using density gradient ultracentrifugation,[26] and purified samples were characterized for electronic-type purity as previously reported.[20,27] A 1:4 ratio of sodium dodecyl sulfate to sodium cholate at an overall surfactant loading of 1% (w/v) was used to isolate HiPco SWCNTs with semiconducting purities of at least 97%. Note that electronic-type purity determination for semiconducting HiPco SWCNTs is restricted to ∼98%, above which discrimination of the metallic M_{11} transitions that overlap with semiconducting S_{22} transitions is limited. The aqueous solutions of surfactant-encapsulated s-SWCNTs were mixed with ethanol, acetone, and isopropanol, subsequently, and vacuum-filtered on a Nylon membrane to remove surfactants and excess density gradient material. The solid-filtered films were dried and peeled off for use in blend solutions. Approximately 1 mg of s-SWCNTs on a 0.75 in. diameter filter was necessary for the film to be thick enough to peel off successfully.

Nanocarbon Blend Solution Preparation. The fullerene derivative (6,6)-phenyl-C_{71}-butyric acid methyl ester ($PC_{71}BM$, American Dye Source) and poly(3-hexylthiophene-2,5-diyl) (P3HT, Ossila) were used as purchased. Solutions of s-SWCNTs in 1,2-DCB were sonicated with P3HT at a ratio of 2:1 SWCNT:polymer. The solution was then filtered to remove large aggregates and combined at a concentration of 2 mg/mL with $PC_{71}BM$ (40 mg/mL) in 1,2-DCB and stirred at 45 °C overnight.

Device Fabrication and Characterization. Polyethylenimine (PEIE, Mw: 70 000 g/mol, Aldrich) was dissolved in water at a concentration of 35−40 wt % and further diluted with 2-methoxyethanol to a weight concentration of 0.4, 1, and 2%. PEIE was spin-coated onto the ZnO nanowire arrays at

DOI: 10.1021/acsami.5b01536
ACS Appl. Mater. Interfaces 2015, 7, 7428−7435

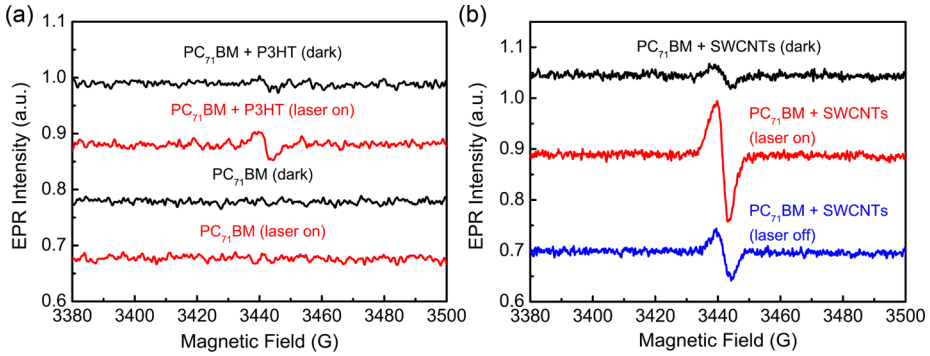

Figure 2. Charge-transfer dynamics in the SWCNT−fullerene blend. (a) EPR and L-EPR spectra containing only $PC_{71}BM$ and blends of $PC_{71}BM$ with 1 wt % P3HT. (b) EPR and L-EPR spectra of $PC_{71}BM$ with 3 wt % SWCNTs and 1 wt % P3HT with the laser on and after the laser was turned off. λ_{exc} = 532 nm, T = 5 K. Spectra were shifted along the y-axis for better visual comparison.

4000 rpm for 1 min to obtain optimal thickness, with varying thickness layers spin-coated at alternative speeds. Active layer solutions were spin-coated onto the PEIE functionalized ZnO nanowire arrays at 600 rpm for 60 s in a N_2-filled glovebox. The substrates were annealed at 120 °C for 10 min to ensure the infiltration of the active layer into the nanowire arrays. MoO_x (5 nm, Aldrich, 99.99% trace metals basis) and 100 nm Ag were thermally evaporated through shadow masks at a base pressure of 5×10^{-6} Torr at rates of 0.1 and 1 Å/s, respectively. The device area was masked and defined by the overlap between the top and bottom electrodes which was 1.2 mm^2. Current density−voltage (J−V) plots were taken by a Keithley source generator under illumination from a calibrated solar simulator (xenon lamp, Newport) with an intensity of 100 mW/cm^2 and an AM1.5 filter. The photoresponsivity and photodetectivity measurements were carried out on a Newport system with an Oriel monochromator (300−700 nm xenon lamp, 700−1100 nm, Tungsten Lamp). For photovoltaic performance measurements, the short circuit current density was corrected based on integration of the external quantum efficiency against the AM1.5G solar spectrum using the Open Photovoltaics Analysis Platform (www.opvap.com). The device cross-section was characterized using a Leo 1550 field emission scanning electron microscope (SEM).

Work Function Measurements. The work function values of the interfaces within the devices were determined by ultraviolet photoelectron spectroscopy (UPS) measurements on a Thermo Scientific ESCALAB 250Xi with a 21.2 eV He(I) source at an energy step size of 0.05 eV, base pressure of 8×10^{-10} mbar, and a pass energy of 2 eV. Gold foil was used to calibrate the instrument. The secondary electron cutoff for the various layers was determined on application of a −10 V sample bias by fitting curves from five measurements of each sample.

3. RESULTS AND DISCUSSION

A schematic structure of an ordered nanocarbon BHJ photovoltaic device is shown in Figure 1a, where the zinc oxide (ZnO) nanowire array (Figures S1 and S2 of the Supporting Information) is grown on an ITO substrate, subsequently coated with PEIE, next infiltrated with the SWCNT−$PC_{71}BM$ blend (Figure S3), capped with a molybdenum oxide (MoO_x) hole-transport layer (HTL), and then a silver (Ag) anode. The nanocarbon BHJ blend features s-SWCNTs purified through density gradient ultracentrifugation (DGU) with a diameter range of 0.8−1.2 nm,[26,28] a broad chiral distribution,[21,29] and semiconducting purity exceeding 97%.[20,21,27] These SWCNTs have previously been shown to result in stable, high-performance SWCNT−fullerene photovoltaics and photodetectors.[7,21] Characteristic dark and illuminated current density−voltage (J−V) curves of the champion nanocarbon BHJ devices are shown in Figure 1b, in which the dark saturation current density (J_d) at zero bias voltage is 3.0×10^{-3} mA/cm^2. The illuminated J−V curve exhibits a photovoltaic response with an open-circuit voltage (V_{oc}) of 0.74 V, a short-circuit current density (J_{sc}) of 10.4 mA/cm^2, a fill factor (FF) of 0.42, and power conversion efficiency of 3.2% under AM 1.5 1 sun illumination. (The average power conversion efficiency gives 2.5% under AM 1.5 1 sun illumination, which is measured over 100 devices.) We previously demonstrated that the performance of these cells is largely determined by the device architecture and morphology, described by nanowire height and electrode work function. The polychiral nature of semiconducting SWCNTs prepared by DGU affords broad-spectral absorption, as seen in Figure 1c. Here, the absorption and external quantum efficiency (EQE) are plotted against each other, showing high absorption in the visible from the fullerene and absorption throughout the near-infrared (NIR) from the SWCNTs. We note that the absorption and EQE spectra deviate beyond 1250 nm, indicating that many of the SWCNT chiralities absorbing at these wavelengths do not have the adequate type-II band alignment with the fullerene to support exciton dissociation and are thus effectively inactive. Furthermore, potential artifacts from the illumination source in the near-IR have been accounted for by comparing EQE response using multiple source lamps (Figure S4).

The wavelength-dependent broad photodetectivity of polychiral s-SWCNTs in the devices upon zero bias voltage is shown in Figure 1d. The photodetectivity (D^*) is calculated based on R_λ and J_d according to eq 1,

$$D^* = \frac{R_\lambda}{(2qJ_d)^{1/2}} \quad (1)$$

where J_d is the dark current, q is the fundamental charge, and R_λ is the wavelength-dependent photoresponsivity. The nanocarbon detector exhibits $D^* > 10^{12}$ Jones from 400 to 650 nm and a peak detectivity of 2×10^{12} Jones at 500 nm, as shown in Figure S5. This detectivity is almost 2 orders of magnitude greater than that of CNT/polymer-based photodetectors (≈3×10^{10} Jones at 500 nm)[30,31] and also exceeds that of low-donor concentration $PC_{71}BM$/P3HT photodetectors (Figure S5). In the NIR range, the photodetectivity of the nanocarbon BHJ

DOI: 10.1021/acsami.5b01536
ACS Appl. Mater. Interfaces 2015, 7, 7428−7435

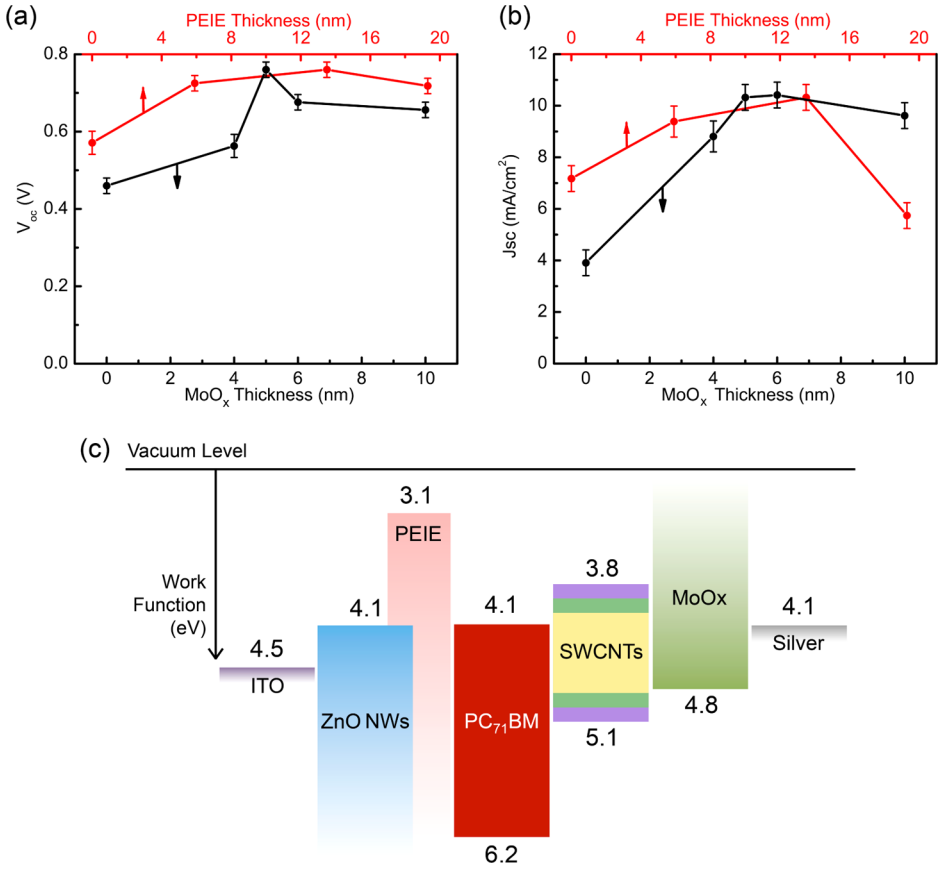

Figure 3. Charge-transfer dynamics at the cathode and anode interfaces. (a) Dependence of V_{oc} on MoO_x and PEIE thickness. (b) Dependence of J_{sc} on MoO_x and PEIE thickness. (c) Proposed flat-band diagram of SWCNT−fullerene BHJ, where the V_{oc} according to the metal−insulator−metal model is determined by the work function difference between MoO_x and ZnO/PEIE.

devices is 1.1×10^{11} Jones (λ = 888 nm), 0.3×10^{11} Jones (λ = 986 nm), and 0.5×10^{11} Jones (λ = 1035 nm), respectively, which is consistent with the photoabsorption spectrum of nanocarbon devices, as shown in Figure 1d. The photodetector performance shows a dependence on applied bias and ZnO nanowire length, as seen in parts a and b of Figure S6, respectively. An optimal ZnO nanowire height of 60 nm is observed,[21] indicative of a balance between enhancement of charge extraction from increased surface area and recombination from the increased surface traps. In comparison to the nanocarbon photodetectors, $PC_{71}BM$/P3HT BHJ devices do not exhibit the same photoresponse under NIR illumination (1100 nm), as shown in Figure 1d and Figure S6c.

Despite recent advances in the photovoltaic and photodetection performance of SWCNT−fullerene BHJs, the details of charge-transfer dynamics in these systems are largely unknown. Additionally, to obtain significantly high concentrations of SWCNTs in organic solvents, dispersant polymers are often used.[6,32−34] In our BHJ blends, we use the hole-conducting polymer poly(3-hexylthiophene-2,5-diyl) (P3HT), which is widely known as an electron donor itself to both fullerenes and SWCNTs.[35−37] To investigate the possible effects of the dispersant polymer in charge transfer, light-induced electron paramagnetic resonance (L-EPR) spectroscopy was used. Figure 2a shows the EPR spectra of $PC_{71}BM$ alone, which displays only noise with and without 532 nm laser photoexcitation. Figure 2a also shows EPR spectra of $PC_{71}BM$ with ∼1 wt % P3HT, the typical amount used to disperse s-SWCNTs in our blends. A weak X-band signal can be seen under dark and illuminated conditions; they come from few charge transfer through $PC_{71}BM$-P3HT bulk heterojunction under very low P3HT concentration.[38] However, both of these signals are far weaker than those seen in the blend of $PC_{71}BM$ + 3 wt % s-SWCNTs + ∼1 wt % P3HT in Figure 2b. Charge-transfer dynamics in the strong L-EPR spectrum under 532 nm photoexcitation in Figure 2b is indicative of polaron formation in the X-band spectrum. This signal likely originates from a negative ($PC_{71}BM^-$) polaron since the DGU-purified s-SWCNTs have been shown to display negligible X-band EPR signals.[39] After switching off the laser source, another EPR spectrum was recorded (blue trace in Figure 2b), and part of the L-EPR signal persists, suggesting the presence of long-lived photoexcited charge carriers. From these data, it is clear that the formation of these carriers depends on the presence of the s-SWCNT donor, not on the low concentrations of the dispersant P3HT polymer. This result contrasts previous experiments where a low concentration of SWCNTs did not significantly affect the EPR signals from a P3HT−SWCNT−PCBM blend.[40] Thus, the blends used in this work are unique in that the SWCNTs behave as the primary donor component rather than P3HT.

We previously demonstrated that the V_{oc} in conventional geometry SWCNT-fullerene BHJ solar cells is best described by the metal−insulator−metal model,[21,41] where the work function offset between the cathode and anode determines the V_{oc} across the cell. In parts a and b of Figure 3, we show the dependence of the V_{oc} and J_{sc} on the PEIE and MoO_x layer thicknesses. In these figures, a fixed MoO_x thickness (5 nm) is

DOI: 10.1021/acsami.5b01536
ACS Appl. Mater. Interfaces 2015, 7, 7428−7435

used while varying the PEIE thickness, and vice versa (where the PEIE thickness is fixed at 13.5 nm). A strong dependence of both parameters on MoO_x and PEIE thicknesses is evident, with a 0.4 V increase in the V_{oc} from no MoO_x to a thickness of 5 nm and an increase of 0.2 V upon the addition of PEIE. As both materials are insulators, performance falls at higher thicknesses (Figure S8), indicating optimal thickness values for each. These trends are similar to ZnO nanowire array-based inorganic quantum dot solar cells,[42] where the differences of optimum thicknesses can be attributed to a smooth nanocarbon active layer. Work function measurements on the electrodes and interfacial layers (Figure S9) lead to the band diagram in Figure 3c. The deep work function of MoO_x greatly modifies the work function of Ag and aligns well with the valence band of the smallest band gap SWCNTs in the blend at 4.8 eV. Note that the work function of MoO_x reported here is measured on a film of MoO_x deposited on silver and exposed briefly to ambient conditions before returning to vacuum during measurement. Previous measurements of the work function of MoO_x have led to values that exceed the work function reported here.[43,44] However, these previous experiments were done on neat MoO_x films that have not been exposed to ambient conditions. In contact with other materials, electron extraction occurs from the MoO_x film, allowing it to behave as a hole-transport material.[43,44] The work function measured here thus represents the effective Fermi level of the contact seen by the BHJ blend in a real device since this extraction has occurred on deposition onto the silver film and on subsequent ambient exposure. Though the PEIE shows a shallow work function and modifies the surface of the ZnO nanowires, a difference of only 0.2 eV is observed since the lowest unoccupied molecular orbital (LUMO) level of $PC_{71}BM$ at 4.1 eV sets a limit on the voltage across the cell. A similarly limited 0.2 eV shift has been observed in other organic photovoltaic blends incorporating $PC_{71}BM$ and ZnO/PEIE.[45] Thus, the inverted architecture adheres to the metal−insulator−metal model, and PEIE and MoO_x of appropriate thicknesses are essential to maximizing device V_{oc}.

To gain more insight into the role of the PEIE-coated ZnO nanowires, the light-intensity dependence of J_{sc} and V_{oc} was studied, as shown in Figure 4a,b. Here, devices with a planar ZnO seed layer, a ZnO nanowire array, and a PEIE-coated ZnO nanowire array are compared. The light-intensity-dependent current J_{sc} in Figure 4a is fit to the power-law relation (eq 2),

$$J_{sc} \propto I^{\alpha} \tag{2}$$

where I is the light intensity and the exponent α is related to charge-transfer dynamics within the system.[23,46] For all three device architectures, α is close to 1, indicating that the short-circuit current is not limited by space-charge effects,[46,47] variations in mobility between the two active layer components,[23] or bimolecular recombination.[22,23] The ZnO nanowire array shows a slightly enhanced current at all intensities over the ZnO planar structure, but the enhancement is much greater when PEIE is coated on the ZnO nanowire structure.

The role of PEIE in current enhancement is clarified with the light-intensity-dependent V_{oc} measurements in Figure 4b. Here, the V_{oc} data are fit to the relation of eq 3,

$$V_{oc} \propto S \ln I \tag{3}$$

where I is the light intensity and S is the slope of the relation. A slope equal to kT/q (≈26 mV at room temperature) is

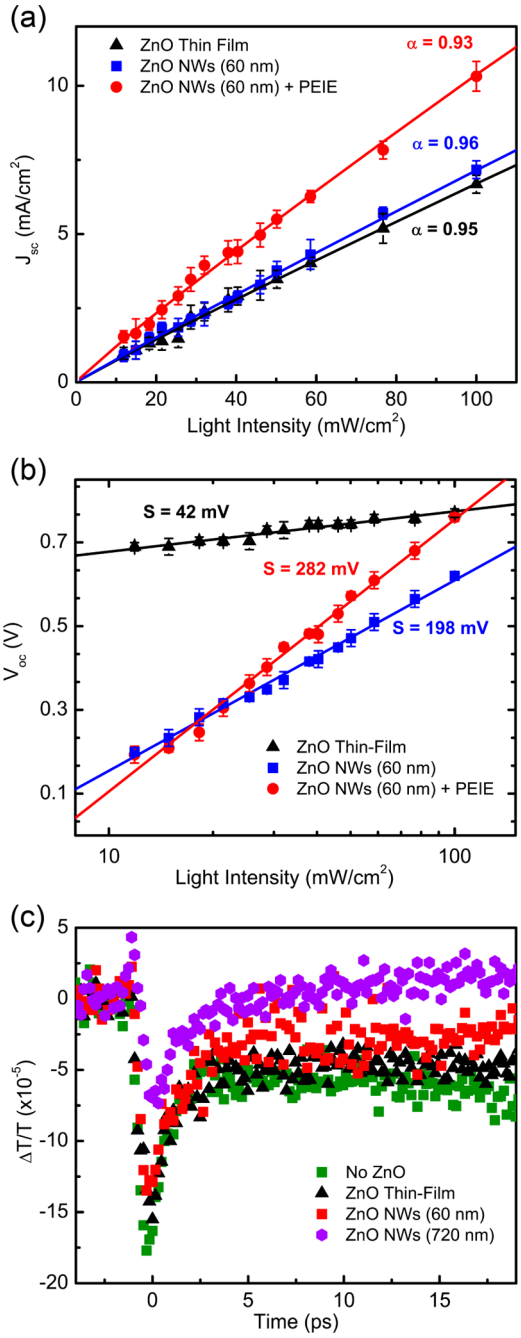

Figure 4. Charge-transfer dynamics at the active layer/ETL interface. Light-intensity dependence of (a) J_{sc} and (b) V_{oc} of SWCNT−fullerene BHJs. (c) Differential transmission signal as a function of probe delay from transient absorption measurements showing increasing carrier lifetime with increasing ZnO nanowire height.

commonly seen in organic donor−acceptor BHJ blends and has been attributed to bimolecular recombination acting as the dominant recombination mechanism under open-circuit conditions.[23] In contrast, conventional silicon photovoltaic cells display a slope of $2kT/q$ (≈52 mV at room temperature), where trap-assisted recombination dominates in the open-circuit case.[23,48] For the ZnO planar device architecture, we observe a slope of 42 mV at room temperature, indicative of trap-assisted recombination within the active layer. This behavior could arise from traps in large fullerene domains or in the percolating network of SWCNTs with various band gaps.

DOI: 10.1021/acsami.5b01536
ACS Appl. Mater. Interfaces 2015, 7, 7428−7435

Reducing such traps in either the SWCNT or fullerene network would likely enhance charge extraction from the blend. In the case of SWCNTs, these data suggest that there may be an optimal collection of SWCNT chiralities with fewer species than the wide distribution presented here. Such a distribution would have more than one chirality to enhance light absorption but would lack the optically inactive chiralities that increase the number of traps in the SWCNT network without contributing to photocurrent. On the basis of the EQE spectrum, the specific chirality combination would be efficient to enhance the photocurrent for the SWCNT−fullerene heterojunctions. For the ZnO nanowire array devices, the slope increases drastically to 200 mV and a reduction in V_{oc} is observed at all light intensities. A similar increase in slope has been observed when incorporating ZnO nanowires in other thin-film photovoltaic technologies and is indicative of an increase in trap-assisted recombination at the interface between the active layer and the ZnO nanowire array.[49] While the ZnO nanowires have enhanced surface area that can enhance charge extraction, the increase in interfacial area also increases the propensity for recombination.

Upon the addition of PEIE, the drop in V_{oc} from increased surface recombination can be overcome, resulting in voltages that reach parity with the planar ZnO layers at higher light intensities. Thus, the data indicate that PEIE suppresses surface recombination from the addition of the ZnO nanowires, enabling their use to enhance charge extraction from the BHJ blend. Figure 4c shows femtosecond pump−probe data for samples with various ZnO nanostructures coated with PEIE.[50] In this measurement, the pump pulse wavelength is 780 nm (within the absorption line of the fullerene and the S_{22} exciton state of the SWCNTs) with an energy fluence of 90 μJ/cm^2. The probe pulse is tuned to 1030 nm, within the absorption line of the lowest exciton state (S_{11}) of the studied SWCNTs. We note that both pulses are far below the band gap energy of ZnO to avoid any direct response from the ZnO ETL. For each sample, the differential transmission of the probe (normalized change of the probe transmission by the pump) is measured as a function of the probe delay time with respect to the pump pulse. Using single-exponential fits to the data, we extract the carrier lifetimes presented in Table 1. PEIE-coated ZnO nanowires enhance the carrier lifetime over the planar structure by successfully suppressing surface recombination at the active layer/ETL interface. This enhancement likely stems from the reduction of the cathode work function (Figure S9) that has previously been shown to reduce the trap-induced recombination.[51]

Table 1. Carrier Lifetimes of PEIE-Coated ZnO Layers with Various Structures

interface material	carrier lifetime (ps)
no ZnO	0.67
ZnO thin film	1.16
ZnO NWs (60 nm)	1.67
ZnO NWs (720 nm)	2.75

4. CONCLUSIONS

In conclusion, we have demonstrated an inverted device architecture of nanocarbon SWCNT−fullerene blends utilizing a ZnO nanowire array that show high photovoltaic and photodetection performance. We studied the charge-transfer dynamics of the blend itself, the cathode and anode interfaces, and the unique ETL involving PEIE-coated ZnO nanowires. We find that the SWCNTs and fullerenes alone rather than the dispersant polymer dominate charge transport, and that the thickness of the cathode and anode surface modifiers must be tuned to maximize the voltage across the cell. Furthermore, we find that trap-assisted recombination dominates in the system, in contrast to bimolecular recombination seen in organic photovoltaics. Thus, further advances in reducing traps within the active layer and at the interfaces is expected to increase performance. Finally, PEIE is shown to effectively passivate the surface traps introduced by the ZnO nanowire network, allowing the high surface area electrode to aid in charge transfer out of the blend. This charge-selective interfacial modification strategy provides a promising pathway for the fabrication of solution-processed nanocarbon optoelectronic devices with high efficiency and long-term stability.

■ ASSOCIATED CONTENT

Supporting Information

SEM images of ZnO nanowire arrays and those infiltrated by a $PC_{71}BM$−SWCNT nanocarbon BHJ; near-IR EQE of SWCNT−fullerene BHJ device; photodetectivity, L-EPR spectra for charge-transfer dynamics of SWCNT−fullerene−ZnO blend; fill factor and power conversion efficiency vs the thickness of MoO_x and PEIE; and ultraviolet photoelectron spectroscopy spectra. This material is available free of charge via the Internet at http://pubs.acs.org.

■ AUTHOR INFORMATION

Corresponding Authors

*E-mail: shenqiang@ku.edu.
*E-mail: m-hersam@northwestern.edu.

Author Contributions

[&]These authors contributed equally. M.G. carried out carbon devices, and T.A.S prepared samples of carbon nanotubes, performed data analysis, and prepared the manuscript. A.R. prepared samples for work function measurements. Q.C. and H.Z. performed ultrafast laser measurement and contributed to the analysis. K.A.L. performed UPS work function measurements and performed analysis on the data. R.R.K. did the electron paramagnetic resonance study and contributed to the analysis. T.J.M., M.F.D., M.C.H., and S.R. supervised the project. All authors gave input on the data analysis and manuscript.

Notes

The authors declare no competing financial interest.

■ ACKNOWLEDGMENTS

Work at the University of Kansas (S.R) was supported by the Army Research Office - Young Investigator Program (W911NF-14-1-0443, material design/self-assembly of carbon heterojunctions), Department of Energy-Basic Energy Sciences Award No. DE-FG02-13ER46937 (organic synthesis and physical property measurement), and National Science Foundation - DMR Award No. 0954486 (H.Z., ultrafast pump−probe measurements). Work at Northwestern University (M.C.H. and T.J.M.) was supported as part of the Argonne−Northwestern Solar Energy Research (ANSER) Center, an Energy Frontier Research Center funded by the U.S. Department of Energy, Office of Science, Basic Energy Sciences under Award No. DE-SC0001059. T.A.S. and K.A.L.

DOI: 10.1021/acsami.5b01536
ACS Appl. Mater. Interfaces 2015, 7, 7428−7435

acknowledge graduate research fellowships from the National Science Foundation. R.R.K. thanks the National Research Council for the Postdoctoral Fellowship. UPS was performed in the NUANCE facility at Northwestern University, which is supported by the NSF-MRSEC (DMR-1121262), Keck Foundation, and State of Illinois.

REFERENCES

(1) Li, C.; Chen, Y. H.; Wang, Y. B.; Iqbal, Z. F.; Chhowalla, M.; Mitra, S. A Fullerene-Single Wall Carbon Nanotube Complex for Polymer Bulk Heterojunction Photovoltaic Cells. *J. Mater. Chem.* **2007**, *17*, 2406−2411.
(2) Wei, L.; Tezuka, N.; Umeyama, T.; Imahori, H.; Chen, Y. Formation of Single-Walled Carbon Nanotube Thin Films Enriched with Semiconducting Nanotubes and Their Application in Photoelectrochemical Devices. *Nanoscale* **2011**, *3*, 1845−1849.
(3) Ramuz, M. P.; Vosgueritchian, M.; Wei, P.; Wang, C. G.; Gao, Y. L.; Wu, Y. P.; Chen, Y. S.; Bao, Z. N. Evaluation of Solution-Processable Carbon-Based Electrodes for All-Carbon Solar Cells. *ACS Nano* **2012**, *6*, 10384−10395.
(4) Bernardi, M.; Lohrman, J.; Kumar, P. V.; Kirkeminde, A.; Ferralis, N.; Grossman, J. C.; Ren, S. Nanocarbon-Based Photovoltaics. *ACS Nano* **2012**, *6*, 8896−8903.
(5) He, M.; Wang, M.; Lin, C.; Lin, Z. Optimization of Molecular Organization and Nanoscale Morphology for High Performance Low Bandgap Polymer Solar Cells. *Nanoscale* **2014**, *6*, 3984−3994.
(6) Ye, Y.; Bindl, D. J.; Jacobberger, R. M.; Wu, M.-Y.; Roy, S. S.; Arnold, M. S. Semiconducting Carbon Nanotube Aerogel Bulk Heterojunction Solar Cells. *Small* **2014**, *10*, 3299−3306.
(7) Xie, Y.; Gong, M.; Shastry, T. A.; Lohrman, J.; Hersam, M. C.; Ren, S. Broad-Spectral-Response Nanocarbon Bulk-Heterojunction Excitonic Photodetectors. *Adv. Mater.* **2013**, *25*, 3433−3437.
(8) Wong, S. S.; Harper, J. D.; Lansbury, P. T.; Lieber, C. M. Carbon Nanotube Tips: High-Resolution Probes for Imaging Biological Systems. *J. Am. Chem. Soc.* **1998**, *120*, 603−604.
(9) Park, H.; Chang, S.; Jean, J.; Cheng, J. J.; Araujo, P. T.; Wang, M.; Bawendi, M. G.; Dresselhaus, M. S.; Bulović, V.; Kong, J.; Gradečak, S. Graphene Cathode-Based ZnO Nanowire Hybrid Solar Cells. *Nano Lett.* **2012**, *13*, 233−239.
(10) Guo, C. X.; Li, C. M. A Self-Assembled Hierarchical Nanostructure Comprising Carbon Spheres and Graphene Nanosheets for Enhanced Supercapacitor Performance. *Energy Environ. Sci.* **2011**, *4*, 4504−4507.
(11) He, Y.; Chen, W.; Gao, C.; Zhou, J.; Li, X.; Xie, E. An Overview of Carbon Materials for Flexible Electrochemical Capacitors. *Nanoscale* **2013**, *5*, 8799−8820.
(12) He, M.; Qiu, F.; Lin, Z. Towards High-Performance Polymer-Based Thermoelectric Materials. *Energy Environ. Sci.* **2013**, *6*, 1352−1361.
(13) Choi, W. B.; Chung, D. S.; Kang, J. H.; Kim, H. Y.; Jin, Y. W.; Han, I. T.; Lee, Y. H.; Jung, J. E.; Lee, N. S.; Park, G. S.; Kim, J. M. Fully Sealed, High-Brightness Carbon-Nanotube Field-Emission Display. *Appl. Phys. Lett.* **1999**, *75*, 3129−3131.
(14) Qi, P.; Vermesh, O.; Grecu, M.; Javey, A.; Wang, Q.; Dai, H.; Peng, S.; Cho, K. J. Toward Large Arrays of Multiplex Functionalized Carbon Nanotube Sensors for Highly Sensitive and Selective Molecular Detection. *Nano Lett.* **2003**, *3*, 347−351.
(15) Shim, B. S.; Chen, W.; Doty, C.; Xu, C.; Kotov, N. A. Smart Electronic Yarns and Wearable Fabrics for Human Biomonitoring Made by Carbon Nanotube Coating with Polyelectrolytes. *Nano Lett.* **2008**, *8*, 4151−4157.
(16) He, M.; Jung, J.; Qiu, F.; Lin, Z. Graphene-Based Transparent Flexible Electrodes for Polymer Solar Cells. *J. Mater. Chem.* **2012**, *22*, 24254−24264.
(17) Lu, L.; Xu, T.; Chen, W.; Lee, J. M.; Luo, Z.; Jung, I. H.; Park, H. I.; Kim, S. O.; Yu, L. The Role of N-Doped Multiwall Carbon Nanotubes in Achieving Highly Efficient Polymer Bulk Heterojunction Solar Cells. *Nano Lett.* **2013**, *13*, 2365−2369.
(18) You, J.; Dou, L.; Yoshimura, K.; Kato, T.; Ohya, K.; Moriarty, T.; Emery, K.; Chen, C.-C.; Gao, J.; Li, G.; Yang, Y. A Polymer Tandem Solar Cell with 10.6% Power Conversion Efficiency. *Nat. Commun.* **2013**, *4*, 1446.
(19) Rath, A. K.; Bernechea, M.; Martinez, L.; de Arquer, F. P. G.; Osmond, J.; Konstantatos, G. Solution-Processed Inorganic Bulk Nano-Heterojunctions and Their Application to Solar Cells. *Nat. Photonics* **2012**, *6*, 529−534.
(20) Tyler, T. P.; Shastry, T. A.; Leever, B. J.; Hersam, M. C. Narrow Diameter Distributions of Metallic Arc Discharge Single-Walled Carbon Nanotubes Via Dual-Iteration Density Gradient Ultracentrifugation. *Adv. Mater.* **2012**, *24*, 4765−4768.
(21) Gong, M.; Shastry, T. A.; Xie, Y.; Bernardi, M.; Jasion, D.; Luck, K. A.; Marks, T. J.; Grossman, J. C.; Ren, S.; Hersam, M. C. Polychiral Semiconducting Carbon Nanotube−Fullerene Solar Cells. *Nano Lett.* **2014**, *14*, 5308−5314.
(22) Koster, L.; Mihailetchi, V.; Blom, P. Bimolecular Recombination in Polymer/Fullerene Bulk Heterojunction Solar Cells. *Appl. Phys. Lett.* **2006**, *88*, 052104.
(23) Cowan, S. R.; Roy, A.; Heeger, A. J. Recombination in Polymer-Fullerene Bulk Heterojunction Solar Cells. *Phys. Rev. B* **2010**, *82*, 245207.
(24) Gao, F.; Li, Z.; Wang, J. P.; Rao, A.; Howard, I. A.; Abrusci, A.; Massip, S.; McNeill, C. R.; Greenham, N. C. Trap-Induced Losses in Hybrid Photovoltaics. *ACS Nano* **2014**, *8*, 3213−3221.
(25) Gong, M.; Xu, X.; Yang, Z.; Liu, Y.; Lv, H.; Lv, L. A Reticulate Superhydrophobic Self-Assembly Structure Prepared by ZnO Nanowires. *Nanotechnology* **2009**, *20* (16), 165602.
(26) Arnold, M. S.; Green, A. A.; Hulvat, J. F.; Stupp, S. I.; Hersam, M. C. Sorting Carbon Nanotubes by Electronic Structure Using Density Differentiation. *Nat. Nanotechnol.* **2006**, *1*, 60−65.
(27) Shastry, T. A.; Morris-Cohen, A. J.; Weiss, E. A.; Hersam, M. C. Probing Carbon Nanotube-Surfactant Interactions with Two-Dimensional DOSY NMR. *J. Am. Chem. Soc.* **2013**, *135*, 6750−6753.
(28) Green, A. A.; Hersam, M. C. Nearly Single-Chirality Single-Walled Carbon Nanotubes Produced Via Orthogonal Iterative Density Gradient Ultracentrifugation. *Adv. Mater.* **2011**, *23*, 2185−2190.
(29) Bachilo, S. M.; Strano, M. S.; Kittrell, C.; Hauge, R. H.; Smalley, R. E.; Weisman, R. B. Structure-Assigned Optical Spectra of Single-Walled Carbon Nanotubes. *Science* **2002**, *298*, 2361−2366.
(30) Arnold, M. S.; Zimmerman, J. D.; Renshaw, C. K.; Xu, X.; Lunt, R. R.; Austin, C. M.; Forrest, S. R. Broad Spectral Response Using Carbon Nanotube/Organic Semiconductor/C60 Photodetectors. *Nano Lett.* **2009**, *9*, 3354−3358.
(31) Gong, X.; Tong, M.; Xia, Y.; Cai, W.; Moon, J. S.; Cao, Y.; Yu, G.; Shieh, C.-L.; Nilsson, B.; Heeger, A. J. High-Detectivity Polymer Photodetectors with Spectral Response from 300 to 1450 nm. *Science* **2009**, *325*, 1665−1667.
(32) Bindl, D.; Brewer, A.; Arnold, M. Semiconducting Carbon Nanotube/Fullerene Blended Heterojunctions for Photovoltaic near-Infrared Photon Harvesting. *Nano Res.* **2011**, *4*, 1174−1179.
(33) Nish, A.; Hwang, J.-Y.; Doig, J.; Nicholas, R. J. Highly Selective Dispersion of Single-walled Carbon Nanotubes Using Aromatic Polymers. *Nat. Nanotechnol.* **2007**, *2*, 640−646.
(34) Shea, M. J.; Arnold, M. S. 1% Solar Cells Derived from Ultrathin Carbon Nanotube Photoabsorbing Films. *Appl. Phys. Lett.* **2013**, *102*, 243101.
(35) Holt, J. M.; Ferguson, A. J.; Kopidakis, N.; Larsen, B. A.; Bult, J.; Rumbles, G.; Blackburn, J. L. Prolonging Charge Separation in P3HT-SWNT Composites Using Highly Enriched Semiconducting Nanotubes. *Nano Lett.* **2010**, *10*, 4627−4633.
(36) Kippelen, B.; Bredas, J.-L. Organic Photovoltaics. *Energy Environ. Sci.* **2009**, *2*, 251−261.
(37) Ren, S.; Bernardi, M.; Lunt, R. R.; Bulovic, V.; Grossman, J. C.; Gradecak, S. Toward Efficient Carbon Nanotube/P3HT Solar Cells: Active Layer Morphology, Electrical, and Optical Properties. *Nano Lett.* **2011**, *11*, 5316−5321.

DOI: 10.1021/acsami.5b01536
ACS Appl. Mater. Interfaces 2015, 7, 7428−7435

(38) Krinichnyi, V. I.; Yudanova, E. I. Light-Induced EPR Study of Charge Transfer in P3HT/$PC_{71}BM$ Bulk Heterojunctions. *J. Phys. Chem. C* **2012**, *116*, 9189−9195.
(39) Zaka, M.; Ito, Y.; Wang, H.; Yan, W.; Robertson, A.; Wu, Y. A.; Rummeli, M. H.; Staunton, D.; Hashimoto, T.; Morton, J. J.; Ardavan, A.; Briggs, G. A.; Warner, J. H. Electron Paramagnetic Resonance Investigation of Purified Catalyst-Free Single-Walled Carbon Nanotubes. *ACS Nano* **2010**, *4*, 7708−7716.
(40) Shames, A. I.; Bounioux, C.; Katz, E. A.; Yerushalmi-Rozen, R.; Zussman, E. Light-Induced Electron Paramagnetic Resonance Evidence of Charge Transfer in Electrospun Fibers Containing Conjugated Polymer/Fullerene and Conjugated Polymer/Fullerene/Carbon Nanotube Blends. *Appl. Phys. Lett.* **2012**, *100*, 113303.
(41) Koster, L.; Mihailetchi, V.; Ramaker, R.; Blom, P. Light Intensity Dependence of Open-Circuit Voltage of Polymer: Fullerene Solar Cells. *Appl. Phys. Lett.* **2005**, *86*, 123509.
(42) Jean, J.; Chang, S.; Brown, P. R.; Cheng, J. J.; Rekemeyer, P. H.; Bawendi, M. G.; Gradečak, S.; Bulović, V. ZnO Nanowire Arrays for Enhanced Photocurrent in PbS Quantum Dot Solar Cells. *Adv. Mater.* **2013**, *25*, 2790−2796.
(43) Kröger, M.; Hamwi, S.; Meyer, J.; Riedl, T.; Kowalsky, W.; Kahn, A. P-Type Doping of Organic Wide Band Gap Materials by Transition Metal Oxides: A Case-Study on Molybdenum Trioxide. *Org. Electron.* **2009**, *10*, 932−938.
(44) Kröger, M.; Hamwi, S.; Meyer, J.; Riedl, T.; Kowalsky, W.; Kahn, A. Role of the Deep-Lying Electronic States of MoO_3 in the Enhancement of Hole-Injection in Organic Thin Films. *Appl. Phys. Lett.* **2009**, *95*, 123301.
(45) Woo, S.; Hyun Kim, W.; Kim, H.; Yi, Y.; Lyu, H.-K.; Kim, Y. 8.9% Single-Stack Inverted Polymer Solar Cells with Electron-Rich Polymer Nanolayer-Modified Inorganic Electron-Collecting Buffer Layers. *Adv. Energy Mater.* **2014**, *4*, 1301692.
(46) Koster, L.; Mihailetchi, V.; Xie, H.; Blom, P. Origin of the Light Intensity Dependence of the Short-Circuit Current of Polymer/Fullerene Solar Cells. *Appl. Phys. Lett.* **2005**, *87*, 203502.
(47) Mihailetchi, V.; Wildeman, J.; Blom, P. Space-Charge Limited Photocurrent. *Phys. Rev. Lett.* **2005**, *94*, 126602.
(48) Brabec, C.; Scherf, U.; Dyakonov, V. *Organic Photovoltaics: Materials, Device Physics, and Manufacturing Technologies*; John Wiley & Sons: New York, 2014; pp 345−373.
(49) Guillén, E.; Azaceta, E.; Peter, L. M.; Zukal, A.; Tena-Zaera, R.; Anta, J. A. ZnO Solar Cells with an Indoline Sensitizer: A Comparison between Nanoparticulate Films and Electrodeposited Nanowire Arrays. *Energy Environ. Sci.* **2011**, *4*, 3400−3407.
(50) Ruzicka, B. A.; Wang, R.; Lohrman, J.; Ren, S.; Zhao, H. Exciton Diffusion in Semiconducting Single-Walled Carbon Nanotubes Studied by Transient Absorption Microscopy. *Phys. Rev. B* **2012**, *86*, 205417.
(51) Lee, B. R.; Jung, E. D.; Nam, Y. S.; Jung, M.; Park, J. S.; Lee, S.; Choi, H.; Ko, S.-J.; Shin, N. R.; Kim, Y.-K.; Kim, S. O.; Kim, J. Y.; Shin, H.-J.; Cho, S.; Song, M. H. Amine-Based Polar Solvent Treatment for Highly Efficient Inverted Polymer Solar Cells. *Adv. Mater.* **2014**, *26*, 494−500.

DOI: 10.1021/acsami.5b01536
ACS Appl. Mater. Interfaces 2015, 7, 7428−7435